

Two-blackbody portraits of radiation from magnetized neutron stars

D. G. Yakovlev^{1*}

¹ *Ioffe Institute, Politekhmicheskaya 26, St Petersburg 194021, Russia*

Accepted . Received ; in original form

ABSTRACT

We study a simple model describing thermal radiation spectra from magnetized neutron stars. The model assumes that a star is nearly spherical and isothermal inside and possesses dipole magnetic fields ($B \lesssim 10^{14}$ G) near the surface, which make the surface temperature distribution non-uniform. We assume further that any surface element emits a blackbody (BB) spectrum with a local effective temperature. We show that such thermal spectra (including phase-resolved) are accurately approximated by simple equivalent two-BB (2BB) models. We introduce and study phase-space maps of 2BB parameters and show that these maps can be useful for interpreting neutron star observations, in which 2BB spectral fits have been done.

Key words: stars: neutron – stars: atmospheres – stars: magnetic fields

1 INTRODUCTION

Thermal radiation of neutron stars is formed in very thin surface layers (of thickness from few centimeters to a few millimeters, as reviewed, e.g. by Potekhin 2014). This radiation contains important information on neutron star parameters (such as mass, radius, chemical composition and magnetic field in surface layers). The information can be inferred by interpreting observations of neutron stars with theoretical atmosphere models or models of radiating condensed surface. These interpretations can also be useful for exploring superdense matter in neutron star interiors (see, e.g., Potekhin 2014; Potekhin et al. 2015a and references therein).

We study thermal radiation, which emerges from stellar interiors of middle-aged isolated neutron star. We neglect non-thermal radiation component (of magnetospheric origin) and the effects of rapid rotation. We will mainly consider simplest emission models of neutron stars which possess purely dipole magnetic fields in the surface layers with typical field strengths $B \lesssim 10^{14}$ G.

The magnetic field can make the surface temperature distribution anisotropic and modify the radiation spectrum (e.g. Potekhin et al. 2015a,b; De Grandis et al. 2021). The anisotropic surface temperature distribution in a middle-aged neutron star is usually created in the so-called heat blanketing envelope (e.g. Beznogov et al. 2021), which thermally insulates a warm and nearly isothermal interior of the star from much cooler surface. This heat blanket is typically much thicker than the atmosphere. We will take the surface temperature distributions from the models of heat blankets (e.g. Potekhin et al. 2003; Ho et al. 2008; Potekhin et al. 2015b, and references therein).

The magnetic field effects on thermal emission from the atmosphere are complicated (see, e.g. Zavlin & Pavlov 2002;

Potekhin et al. 2015a; González Caniulef et al. 2016). The radiation can be strongly polarized, contain specific spectral and angular features; it can be greatly variable over the surface. The radiation flux detected by a distant observer must be calculated by integration over the visible part of the surface, taking into account gravitational redshift and light bending of photons.

The progress in developing the magnetized atmospheric models of neutron stars has been reviewed, for instance, by Potekhin (2014); Potekhin et al. (2015a). Such models can be separated into those with a pure radial magnetic field constant on the surface and those with more realistic magnetic fields varying over the surface. The first models are easier to construct but seem less realistic; we will not discuss them. We focus on the atmosphere models with the dipole field configuration which are not numerous (e.g. Ho et al. 2008; Zyuzin et al. 2021). We consider a simplified version of such models, in which any local element on the stellar surface (with non-uniform temperature distribution) emits like a blackbody (BB) with its own local surface temperature T_s , meaning an overall multi-BB thermal radiation. The model was put forward long ago (Greenstein & Hartke 1983) and analyzed in the literature (e.g. Page 1995; Page & Sarmiento 1996; Potekhin & Yakovlev 2001; Potekhin et al. 2003; Geppert et al. 2006; Zane & Turolla 2006). Our main goal will be to study its approximation by a two-BB (2BB) model, a widely used tool for investigating neutron-star radiation.

In Sect. 2 we outline a general multi-BB radiation model for a neutron star with isothermal interiors and dipole surface magnetic field. In Sect. 3 we study spectral fluxes emitted from such a star. We show that these fluxes can accurately be fitted by 2BB models and analyse the dependence of fit parameters on the mean effective temperature of the star, magnetic field strength, and stellar compactness. Also, we derive accurate 2BB fits for any observation direction. We summarize the results and conclude in Sect. 4.

* E-mail: yak.astro@mail.ioffe.ru

2 THEORETICAL MULTI-BB SPECTRA

2.1 Theoretical outline

Let us outline standard calculation of radiation from a spherical neutron star with *any* (not necessarily axially symmetric) non-uniform surface temperature distribution, assuming that any surface element emits a BB radiation with an effective (local, non-redshifted) surface temperature T_s , resulting in multi-BB emission. Since neutron stars are compact, one needs to account for gravitational light bending and redshift in Schwarzschild space-time. These effects are characterized by the neutron star compactness parameter

$$x_g = \frac{r_g}{R}, \quad r_g = \frac{2GM}{c^2}, \quad (1)$$

where M is a gravitational stellar mass, R is a circumferential radius, r_g is the Schwarzschild radius, G is the gravitational constant and c is the speed of light. We will use physical quantities either in a local reference frame near the neutron star surface or in the frame of a distant observer. The latter will be often marked by the symbol ∞ . For instance, $T_s^\infty = \sqrt{1-x_g}T_s$, and the ‘apparent’ neutron star radius for a distant observer is $R_\infty = R/\sqrt{1-x_g}$.

The observer detects the radiative spectral flux density F_∞ [erg cm⁻² s⁻¹ keV⁻¹] at a distance $D \gg R$ per unit interval of the redshifted photon energy $E \equiv E_\infty$. The flux depends on E and observation direction (along a unit vector \mathbf{k}). Let us take a surface element dS of the atmosphere and specify its position either by ordinary spherical angles ϑ and φ (with respect to the magnetic axis) or by the unit vector \mathbf{n} normal to the surface. Then $dS = R^2 d\Omega_s$, with $d\Omega_s = \sin \vartheta d\vartheta d\varphi$ being a solid angle element measured from the stellar centre. The contribution of this element to flux density is (e.g. [Beloborodov 2002](#), [Poutanen & Gierliński 2003](#) and [Potekhin 2014](#))

$$dF_E^\infty = I(E, \mathbf{k}_0) \mathcal{P} \frac{dS}{D^2}, \quad \mathcal{P} = \cos \theta \left| \frac{d \cos \theta}{d \cos \theta_0} \right|, \quad (2)$$

\mathbf{k}_0 being the unit vector along the propagation of those photons in the atmosphere, which are registered by the observer. The directions of \mathbf{k} and \mathbf{k}_0 differ because of gravitational line bending. Furthermore, let θ (or θ_0) be the angle between \mathbf{k} (or \mathbf{k}_0) and the line from the stellar centre to the observer. For given \mathbf{n} and \mathbf{k} , \mathbf{k}_0 is determined by kinematics of light bending. Next, $I(E, \mathbf{k}_0)$ is the radiative intensity emitted in the atmosphere and redshifted for the observer. Finally, \mathcal{P} corrects the intensity of the observed flux due to light bending; it depends on θ , θ_0 and x_g . Any surface element dS is visible by the observer if $\theta \leq \pi/2$. Neglecting the light bending, one has $\theta = \theta_0$ and $\mathcal{P} = \cos \theta$.

Using equation (2) and integrating over dS , one obtains

$$F_E^\infty = \frac{R^2}{D^2} H_E^\infty, \quad H_E^\infty = \int_{\text{viz}} I(E, \mathbf{k}_0) \mathcal{P} d\Omega_s, \quad (3)$$

where H_E^∞ is the effective spectral thermal flux (formally independent of D and R) in the direction of \mathbf{k} . The intergration over $d\Omega_s$ is carried over the visible part of the stellar surface. In our case, the gravitational redshift and light bending are decoupled. The light bending enlarges the observable emission area. It allows one to observe the emission from the opposite side of the star. Note that we neglect photon absorption by intervening matter along propagation path, which will be discussed later.

A local radiation intensity $I_0(E_0)$ of any surface element is given by the Planck function with a local non-redshifted surface temperature $T_s(\mathbf{n})$ and non-redshifted photon energy $E_0 \equiv$

$E/\sqrt{1-x_g}$. Redshifting I_0 and E_0 , from equation (3) we obtain

$$H_E^\infty = \frac{15\sigma_{\text{SB}}}{16\pi^5 k_B^4} \int_{\text{viz}} d\Omega_s \frac{(1-x_g)^{-1} \mathcal{P} E^3}{\exp(E/k_B T_s^\infty) - 1}, \quad (4)$$

where σ_{SB} is the Stefan–Boltzmann constant. Using accurate analytic approximations of \mathcal{P} derived by [Poutanen \(2020\)](#) [his equations (12) and (13)], one can easily compute H_E^∞ for any surface temperature distribution $T_s(\mathbf{n})$ and observation direction \mathbf{k} . In addition, one can calculate the total thermal bolometric luminosity of the star, L_s , and introduce an overall non-redshifted effective surface temperature T_{eff} according to (e.g. [Potekhin & Yakovlev 2001](#))

$$L_s = \sigma_{\text{SB}} R^2 \int_{4\pi} d\Omega_s T_s^4(\mathbf{n}) \equiv 4\pi \sigma_{\text{SB}} R^2 T_{\text{eff}}^4. \quad (5)$$

Here one should integrate over the entire stellar surface.

In addition to the exact effective flux H_E^∞ in the direction of \mathbf{k} , which is given by equation (4), one can introduce the flux $H_E^{\text{av}\infty}$, averaged over orientations of \mathbf{k} at a fixed distance D ,

$$H_E^{\text{av}\infty} = \frac{1}{4\pi} \int_{4\pi} d\Omega_{\mathbf{k}} H_E^\infty, \quad (6)$$

where $d\Omega_{\mathbf{k}}$ is a solid angle element of possible orientations \mathbf{k} of the detector on the sky. The angle-averaging simplifies the integration,

$$H_E^{\text{av}\infty} = \frac{15\sigma_{\text{SB}}}{16\pi^5 k_B^4} \int_{4\pi} d\Omega_s \frac{(1-x_g)^{-1} E^3}{\exp(E/k_B T_s^\infty) - 1}; \quad (7)$$

the angle-averaged bolometric flux determines the total luminosity (5) of the star, $L_s^\infty = 4\pi D^2 F_{\text{bol}}^{\text{av}\infty} = 4\pi \sigma_{\text{SB}} R_\infty^2 T_{\text{eff}}^{\infty 4}$.

For a uniform surface temperature distribution, one naturally recovers the ordinary BB(\equiv 1BB) law,

$$H_E^{\text{BB}\infty} = \frac{15\sigma_{\text{SB}}}{4\pi^4 k_B^4} \frac{(1-x_g)^{-1} E^3}{\exp(E/k_B T_{\text{eff}}^\infty) - 1}, \quad (8)$$

and the bolometric effective flux

$$H_{\text{bol}}^{\text{BB}\infty} = \int_0^\infty H_E^{\text{BB}\infty} dE = \frac{\sigma_{\text{SB}} T_{\text{eff}}^{\infty 4}}{1-x_g}, \quad (9)$$

with $L_s^\infty = 4\pi D^2 F_{\text{bol}}^{\text{BB}\infty} = 4\pi \sigma_{\text{SB}} R_\infty^2 T_{\text{eff}}^{\infty 4}$.

2.2 Illustrative examples

For illustration, Fig. 1 shows (by solid lines) the surface temperature distribution for a passively cooling magnetized neutron star with pure dipole magnetic field in the outer layers, assuming $M = 1.4 M_\odot$ and $R = 12$ km [$x_g=0.344$ and the surface gravity $g_s = GM/(R^2 \sqrt{1-x_g}) = 1.59 \times 10^{14}$ cm s⁻²]. The surface field at the magnetic pole is $B_{\text{pole}} = 10^{14}$ G. The plots are given by the standard theory of magnetized heat blanketing envelopes (e.g., [Potekhin & Yakovlev 2001](#); [Potekhin et al. 2003](#); [Potekhin & Chabrier 2018](#); [Beznogov et al. 2021](#)). The T_s distributions are axially symmetric with respect to the magnetic axis and equator. It is sufficient to plot T_s versus colatitude ϑ from $\vartheta = 0$ (magnetic pole) to 90° (equator). We present the solid curves for seven effective temperatures T_{eff} . The respective dotted curves are for a toy model of heat blankets considered in Sect. 3.6.

The star is assumed to be isothermal inside. The main temperature gradient and the $T_s(\mathbf{n})$ distribution (solid lines) are mediated by heat transport through a thin outer heat blanketing envelope, which extends from the surface to the density $\rho_b \sim 10^{10}$ g cm⁻³. For certainty, unless the contrary is indicated, the blanketing envelope is assumed to be made of iron. The magnetic field makes heat transport anisotropic and creates variations of $T_s(\mathbf{n})$, which

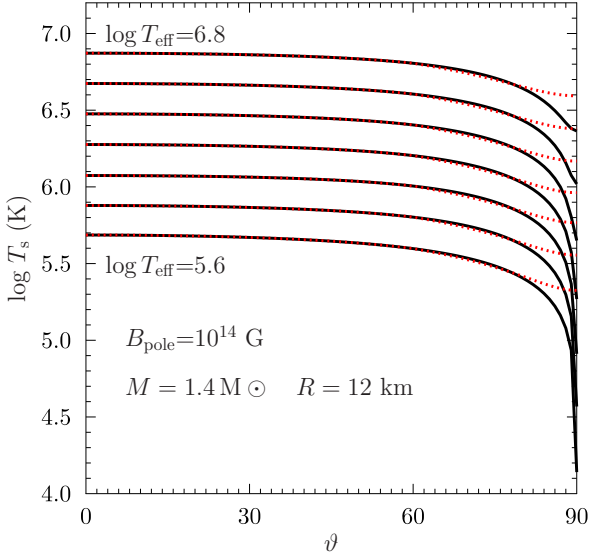


Figure 1. Logarithm of the surface temperature T_s versus colatitude ϑ , from magnetic pole ($\vartheta = 0$) to equator ($\vartheta = 90^\circ$) of a neutron star with $M = 1.4 M_\odot$ and $R = 12$ km at $B_{\text{pole}} = 10^{14}$ G. The curves are plotted for seven effective temperatures, $\log T_{\text{eff}} [\text{K}] = 5.6, 5.8, \dots, 6.8$. Solid curves refer to the basic heat-blanket model (Potekhin & Yakovlev 2001; Potekhin et al. 2003; Potekhin & Chabrier 2018), while dots display an artificial model discussed in Sect. 3.6. See the text for details.

become noticeable at $B_{\text{pole}} \gtrsim 10^{11}$ G. In Fig. 1 displays strong pole-to-equator T_s variations (solid lines) exceeding one order of magnitude at $\log T_{\text{eff}} [\text{K}] = 5.6$. The pole is hotter than the equator because of higher heat conduction in the polar regions, where the heat outflows to the surface nearly along magnetic field lines. In contrast, there is a colder equatorial belt, where the heat outflows nearly across magnetic lines; such outflow is strongly suppressed. In a hotter star with higher T_{eff} , the T_s anisotropy is less pronounced due to reduction of heat transport anisotropy in warmer matter. With increasing B_{pole} , the polar regions become warmer, while the equatorial belt colder and thinner.

Fig. 2 shows the thermal spectral flux density H_E^∞ emitted by same star as in Fig. 1 (for the same seven values of T_{eff} displayed by solid lines). The flux is plotted in logarithmic scale as a function of decimal logarithm of the redshifted photon energy E . For each value of T_{eff} we present three curves. The solid curves give the flux $H_E^{\parallel\infty}$, as measured in pole observations (marked as \parallel , with the inclination $i = 0$ to the magnetic axis). The dashed curves present the flux $H_E^{\perp\infty}$ for the equator observations (marked with \perp , at $i = 90^\circ$). The dotted curves demonstrate the plain 1BB model, equation (8), with given $T_s = T_{\text{eff}}$ constant over the surface. The angle-averaged curves $H_E^{\text{av}\infty}$, given by equation (6), always lie between $H_E^{\parallel\infty}$ and $H_E^{\perp\infty}$ and would be indistinguishable from the dotted curves in the logarithmic format.

All four fluxes for each T_{eff} look very close in the logarithmic format of Fig. 2. To demonstrate their difference, Fig. 3 plots spectral fluxes H_E^∞ in natural format. Here we take $\log T_{\text{eff}} = 6.4$ and express all H_E^∞ in units of $H_E^{\parallel\infty}$. This normalization gives the unit relative flux (solid black line) for pole observations. The flux for the equator observations (long-dashed black line) is always lower because the observer detects radiation emitted from overall colder regions. The $H_E^{\perp\infty}/H_E^{\parallel\infty}$ ratio is seen to decrease with photon

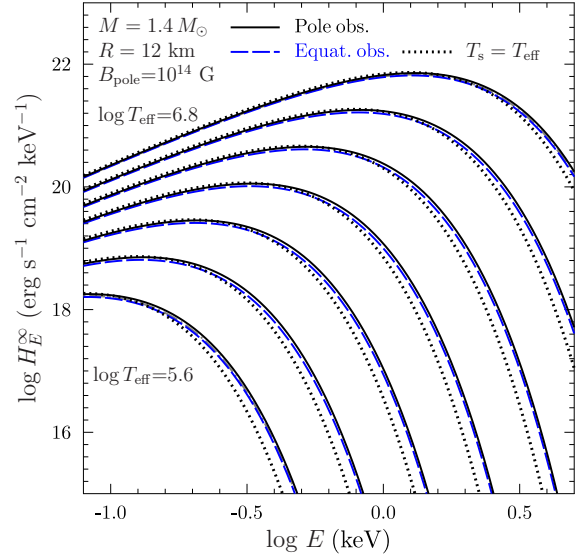


Figure 2. Effective spectral flux density H_E^∞ versus redshifted photon energy E at (from bottom to top) $\log T_{\text{eff}} [\text{K}] = 5.6, 5.8, \dots, 6.8$ from a $1.4 M_\odot$ neutron star with $R = 12$ km and $B_{\text{pole}} = 10^{14}$ G (as in Fig. 1). Solid lines refer to pole observations (inclination angle $i = 0$), dashed lines to equator observations ($i = 90^\circ$); dotted lines are for the 1BB model with given T_{eff} .

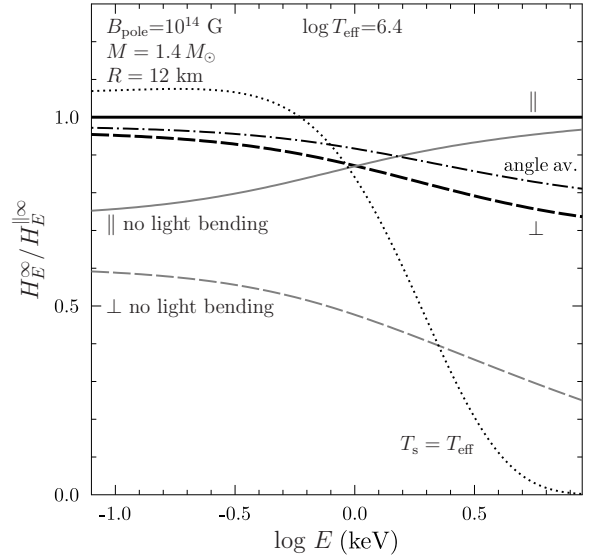


Figure 3. Effective spectral flux density H_E^∞ in units of $H_E^{\parallel\infty}$ versus redshifted photon energy E at $\log T_{\text{eff}} [\text{K}] = 6.4$ for a $1.4 M_\odot$ neutron star with $R = 12$ km and $B_{\text{pole}} = 10^{14}$. Solid lines refer to pole observations, dashed lines to equator observations; dot-dashed line shows the angle-averaged flux, while the dotted line is for the 1BB ($T_s = T_{\text{eff}}$) model. Grey solid and dashed lines are the same fluxes $H_E^{\parallel\infty}$ and $H_E^{\perp\infty}$, as the black lines, but neglecting the gravitational light bending of photons.

energy. The black dash-dot line refers to $H_E^{\text{av}\infty}$, while the dotted black line to $H_E^{\text{BB}\infty}$. One can see that these lines become noticeably different at higher E . Finally, the grey solid and long-dash curves refer to the same $H_E^{\parallel\infty}$ and $H_E^{\perp\infty}$ fluxes, as the black curves, but calculated neglecting gravitational light bending. These grey curves are systematically lower than their black counterparts because the neglect of light bending decreases observable surface area of the star. This confirms the importance of light bending. Note also that the light bending greatly reduces the difference of fluxes in the pole and equator observations, making the thermal neutron star radiation more isotropic (Page 1995).

3 2BB APPROXIMATION

3.1 2BB fits

Here we show that the multi-BB fluxes discussed in Sect. 2.2 can be accurately fitted by a simple 2BB model. The idea is not new (e.g. Popov et al. 2017) but, to the best of our knowledge, it has not been studied in great details. Let us take the same model of a spherical neutron star with a dipole magnetic field near the surface. We have calculated the spectral flux H_E^∞ from equation (4) for a number of values of M , R , B_{pole} , T_{eff} and inclination angles i . We have mainly considered photon energies E from 0.064 keV to $E_{\text{max}} = 42.49$ keV (overlapping thus typical observable X-ray range) on a grid of 142 energy points placed logarithmically equidistant within this range. The spectra have been fitted by the 2BB model,

$$H_E^\infty = s_c H_E^{\text{BB}\infty}(T_{\text{effc}}) + s_h H_E^{\text{BB}\infty}(T_{\text{effh}}). \quad (10)$$

Here $H_E^{\text{BB}\infty}(T_{\text{eff}})$ is given by equation (8), with $T_{\text{effc}} = p_c T_{\text{eff}}$ and $T_{\text{effh}} = p_h T_{\text{eff}}$; the subscripts ‘c’ and ‘h’ refer to the colder and the hotter BB components, respectively. Four positive dimensionless fit parameters s_c , s_h , p_c and p_h define relative contributions of the two BB components to the total thermal flux H_E^∞ . The parameters p_c and p_h determine the effective temperatures of the components, while s_c and s_h are effective fractions of their surface areas (without imposing $s_c + s_h = 1$). Since the first component is colder, we have $p_c < p_h$. We treat $s_{c,h}$ and $p_{c,h}$ just as formal fit parameters (not the parameters of real colder and hotter uniform areas on the neutron star surface). Very roughly, one can visualize $R_c = R \sqrt{s_c}$ and $R_h = R \sqrt{s_h}$ as the effective radii of the colder and hotter emission regions, respectively. All four fit parameters s_c , s_h , p_c and p_h depend on M , R , B_{pole} , T_{eff} and i . Actually, these fit parameters are not independent. They should guarantee the required bolometric luminosity of the star, that is determined by given T_{eff} in accord with equation (5). We used this equation to check the quality of our 2BB fits and it always worked well.

3.2 2BB fits: pole and equator observations

We start with the two basic models for pole and equator observations ($H_E^{\parallel\infty}$ and $H_E^{\perp\infty}$, $i = 0$ and 90°), leaving the case of arbitrary i to Sect. 3.3.

For example, Table 1 presents the fit results for the star with $M = 1.4 M_\odot$ and $R = 12$ km. The fitting has been performed on the indicated grid of 142 energy points E . Before fitting, we have removed the energy points, at which $H_E^\infty < 1 \text{ erg s}^{-1} \text{ cm}^{-2}$ keV $^{-1}$ and the spectral flux is negligible. Table 1 gives the best fit parameters p_c , p_h , s_c and s_h for magnetic pole (\parallel) and equator (\perp) observations at four values of $B_{\text{pole}} = 10^{11}$, 10^{12} , 10^{13} and 10^{14} G. For each B_{pole} , we consider 6×2 atmosphere models with

$\log T_{\text{eff}} [\text{K}] = 5.6, 5.8, \dots, 6.6$ (6 lines with eight fit parameters for any T_{eff} in Table 1). In each line, we present also decimal logarithm of the internal temperature $\log T_b$ and two root mean squared relative fit errors δ_{rms} (for the two observation directions, \parallel and \perp). One can see that in all 48 fit cases δ_{rms} does not exceed 2.5 per cent. The maximum relative fit error is typically $\approx (2 - 2.5) \delta_{\text{rms}}$. Such fits can be regarded as nearly perfect (‘too accurate’), taking into account simplified nature of the initially calculated fluxes. If plotted on Figs. 2 and 3, these fits would be indistinguishable from corresponding solid and long-dashed curves.

3.3 2BB fits: any observation angle

In case of arbitrary inclination i , the spectral flux $H_E^\infty = H_E^{i\infty}$ can be computed from equation (4). We have performed such computations for a range of values of M , R , B_{pole} , T_{eff} and i . In all the cases the computed fluxes $H_E^{i\infty}$ are nicely approximated by

$$H_E^{i\infty} = H_E^{\parallel\infty} \cos^2 i + H_E^{\perp\infty} \sin^2 i, \quad (11)$$

where $H_E^{\parallel\infty}$ and $H_E^{\perp\infty}$ are the fluxes for the pole and equator observations, discussed above. The fit accuracy of equation (11) is of the same order of magnitude as the 2BB fit accuracy of equation (10). Therefore, any thermal spectral flux $H_E^{i\infty}$ observed at any direction i is determined by the two basic pole and equatorial spectral fluxes, $H_E^{\parallel\infty}$ and $H_E^{\perp\infty}$, which are accurately described by 2BB fits with easily computable fit parameters (Table 1). This gives practical solution for the assumed model of magnetized neutron star emission. Note that equation (11) is the same as the equation for the flux produced by a classic electric dipole emission in flat space.

3.4 2BB phase-space maps

Many observed thermal X-ray spectra of neutron stars have been fitted by 2BB models. Since 2BB models accurately approximate a wide class of multi-BB models, it seems attractive to develop a technique for studying properties of magnetized stars, as multi-BB emitters, using already available 2BB fits of the observed spectra. This can be done by comparing theoretical 2BB maps (2BB parameters calculated in a wide phase-space of input parameters, such as M , R , B_{pole} , T_{eff} , i), with observations and selecting then most suitable phase-space domains.

Some maps are demonstrated in Fig. 4. The figure refers to a $1.4 M_\odot$ star with $R = 12$ km and $B_{\text{pole}} = 3 \times 10^{13}$ G, observed from the pole. The fit parameters are displayed versus T_{eff} . The left-hand side plots emitting fractions of the cold and hot BB surface areas, s_c and s_h (lower and upper shaded areas, respectively). For any T_{eff} we have $s_c + s_h < 1$, which may be viewed as the presence of ‘non-emitting’ fraction of the stellar surface shown as blank. This effect supports common knowledge that one should be careful in using s_c and s_h for estimating true neutron star radius from observations. Notice that the presence of the ‘dark’ surface does not affect excellent quality of the 2BB fits. With increasing T_{eff} , the fraction of BB ‘dark’ surface decreases.

The right-hand panel of Fig. 4 shows characteristic temperatures of the emitting star. The shaded zone is restricted by the maximum temperature T_{pole} at the magnetic pole and the minimum temperature T_{eq} at the equator. We see that temperature variations over the surface of a magnetized star are large. The dotted curve plots the mean effective temperature T_{eff} (to guide the eye). The dashed and solid curves are the effective BB temperatures, T_{effh} and T_{effc} , respectively.

Table 1. Fit parameters p_c , p_h , s_c and s_h in equation (10), together with rms relative fit errors δ_{rms} , for a neutron star with $M = 1.4 M_\odot$, $R = 12$ km at two observation directions (\parallel and \perp), four values of $\log B_{\text{pole}}$ [G]=11, 12, 13, 14, and six values of $\log T_{\text{eff}}$ [K]=5.6, 5.8, . . . , 6.6 (with corresponding logarithms of the internal temperature, $\log T_b$ [K]).

$\log B_{\text{pole}}$	$\log T_s$	$\log T_b$	$p_{c\parallel}$	$p_{h\parallel}$	$s_{c\parallel}$	$s_{h\parallel}$	$\delta_{\text{rms}}^{\parallel}$	$p_{c\perp}$	$p_{h\perp}$	$s_{c\perp}$	$s_{h\perp}$	$\delta_{\text{rms}}^{\perp}$
11	5.6	7.3854	0.9708	1.1262	0.5126	0.3669	0.011	0.9624	1.1239	0.5620	0.3002	0.014
11	5.8	7.7477	0.9552	1.1014	0.5641	0.3898	0.009	0.9493	1.0991	0.6258	0.3218	0.011
11	6.0	8.0979	0.9591	1.0750	0.5793	0.4062	0.005	0.9553	1.0729	0.6453	0.3384	0.006
11	6.2	8.4447	0.9685	1.0506	0.5696	0.4269	0.002	0.9663	1.0488	0.6360	0.3601	0.002
11	6.4	8.7918	0.9775	1.0313	0.5426	0.4569	0.001	0.9761	1.0297	0.6046	0.3950	0.001
11	6.6	9.1410	0.9860	1.0191	0.5309	0.4690	0.000	0.9853	1.0180	0.5931	0.4069	0.000
12	5.6	7.3488	1.0057	1.1628	0.4465	0.3312	0.011	0.9952	1.1605	0.4757	0.2667	0.014
12	5.8	7.7410	0.9845	1.1572	0.4682	0.3526	0.014	0.9743	1.1546	0.5055	0.2863	0.018
12	6.0	8.1185	0.9622	1.1490	0.4945	0.3734	0.017	0.9523	1.1463	0.5406	0.3060	0.021
12	6.2	8.4868	0.9435	1.1359	0.5281	0.3913	0.017	0.9348	1.1331	0.5836	0.3231	0.021
12	6.4	8.8435	0.9398	1.1158	0.5582	0.4022	0.013	0.9330	1.1132	0.6209	0.3335	0.016
12	6.6	9.1898	0.9485	1.0895	0.5735	0.4108	0.007	0.9440	1.0872	0.6397	0.3423	0.009
13	5.6	7.2925	1.0032	1.1590	0.4312	0.3461	0.011	0.9933	1.1567	0.4616	0.2799	0.013
13	5.8	7.6673	0.9901	1.1646	0.4613	0.3434	0.014	0.9794	1.1621	0.4955	0.2776	0.018
13	6.0	8.0568	0.9767	1.1642	0.4818	0.3500	0.017	0.9658	1.1616	0.5203	0.2840	0.021
13	6.2	8.4502	0.9621	1.1590	0.4923	0.3659	0.019	0.9515	1.1563	0.5360	0.2989	0.023
13	6.4	8.8348	0.9476	1.1527	0.5025	0.3824	0.020	0.9375	1.1499	0.5513	0.3146	0.024
13	6.6	9.2082	0.9347	1.1452	0.5176	0.3968	0.019	0.9253	1.1422	0.5719	0.3284	0.024
14	5.6	7.1730	1.0225	1.1914	0.4613	0.2819	0.013	1.0095	1.1891	0.4807	0.2230	0.016
14	5.8	7.6315	0.9956	1.1718	0.4702	0.3268	0.015	0.9840	1.1692	0.5017	0.2629	0.018
14	6.0	7.9913	0.9742	1.1603	0.4688	0.3629	0.016	0.9637	1.1576	0.5084	0.2958	0.020
14	6.2	8.3648	0.9650	1.1644	0.4896	0.3589	0.019	0.9539	1.1616	0.5315	0.2922	0.023
14	6.4	8.7685	0.9561	1.1632	0.5022	0.3636	0.020	0.9449	1.1603	0.5469	0.2968	0.025
14	6.6	9.1668	0.9456	1.1580	0.5064	0.3774	0.020	0.9350	1.1550	0.5547	0.3099	0.025

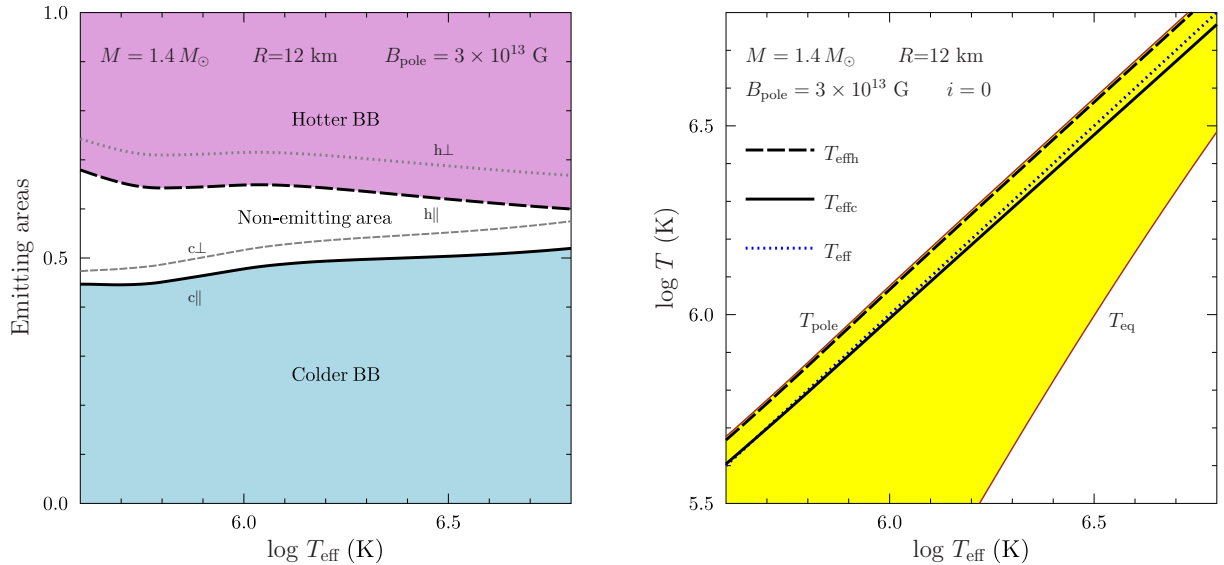


Figure 4. Map of 2BB fit parameters versus $\log T_{\text{eff}}$ for a $1.4 M_\odot$ neutron star with $R = 12$ km and $B_{\text{pole}} = 3 \times 10^{13}$ G for pole observation ($i = 0$). The left-hand panel shows the fractional surface areas s_h and s_c for the hotter and colder BB components as lengths of segments of vertical lines at given T_{eff} in the upper and lower shaded zones, respectively. The blank intermediate zone gives ‘non-emitting’ fractional surface area. The short-dashed and dotted grey lines show the boundaries of the shaded zones for the equator observation ($i = 90^\circ$). The right-hand panel demonstrates characteristic temperatures. The shaded zone shows range of T_s -variations over the surface, from the highest temperature T_{pole} at the pole to the lowest one T_{eq} at the equator. The dotted line is the total effective temperature T_{eff} , while the dashed and solid lines are the effective temperatures T_{effh} and T_{effc} for the hotter and colder BB components (which are almost insensitive of i). See the text for details.

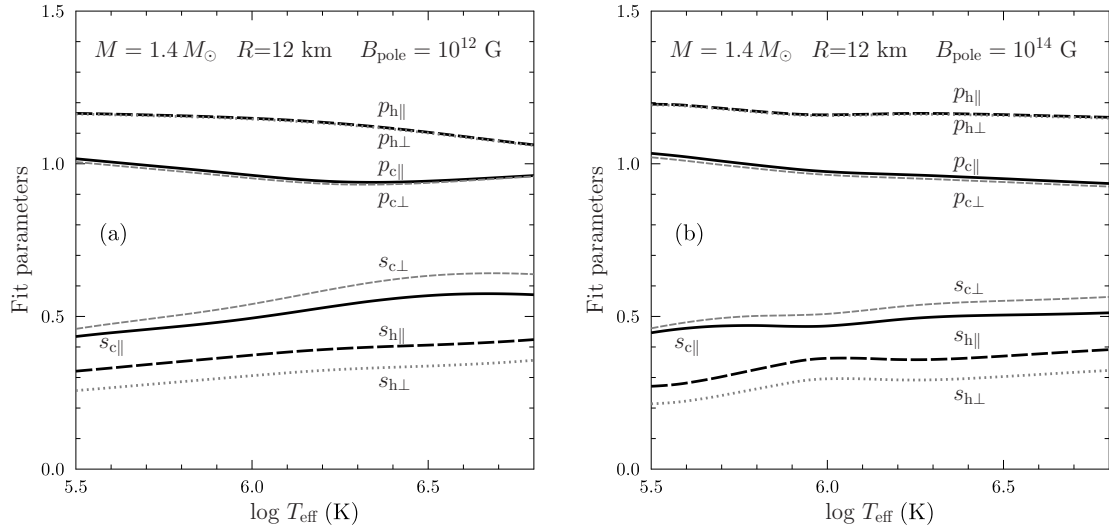


Figure 5. 2BB fit parameters versus $\log T_{\text{eff}}$ for a $1.4 M_{\odot}$ neutron star with $R = 12$ km and $B_{\text{pole}} = 10^{12}$ [panel (a)] or 10^{14} G [panel (b)]. Black and grey lines refer, respectively, to pole and equator observations. Black solid lines show $p_{c\parallel}$ and $s_{c\parallel}$ (for the colder BB components), while black long-dashed lines show $p_{h\parallel}$ and $s_{h\parallel}$ (for the hotter BB components). Short-dashed grey lines refer to $p_{c\perp}$ and $s_{c\perp}$, whereas dotted grey lines to $p_{h\perp}$ and $s_{h\perp}$.

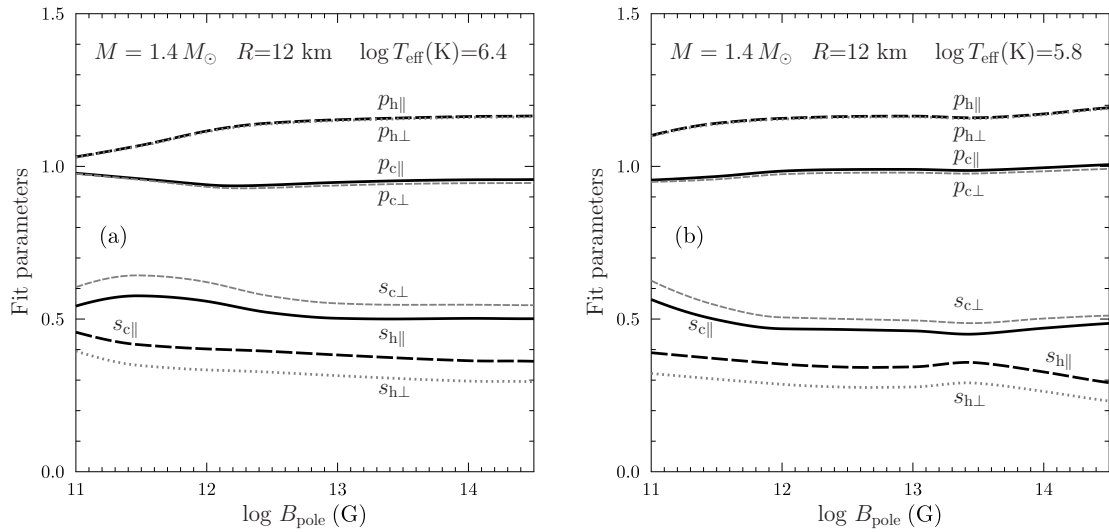


Figure 6. Same 2BB fit parameters as in Fig. 5 for a $1.4 M_{\odot}$ neutron star with $R = 12$ km but versus B_{pole} at $\log T_{\text{eff}}[\text{K}]=6.4$ [panel (a)] and 5.8 [panel (b)]. See the text for details.

Although Fig. 4 is designed for the pole observations, the grey lines on the left-hand panel show the deformations of the emitting zones for the equator observations; these deformations are not dramatic but noticeable. Corresponding deformations on the right-hand panel are not plotted; they would be almost invisible.

Phase-space maps like those in Fig. 4 are convenient but take much space. We will use a more economic format, which allows plotting all four fit parameters on one panel. Fig. 5 demonstrates the behavior of fit parameters (Table 1) versus T_{eff} of the colder and hotter BB components from the star with the same M and R at $B_{\text{pole}} = 10^{12}$ and 10^{14} G [panels (a) and (b), respectively]. The fits for the pole observations are plotted in black, while those for the equator observations are plotted in grey. The upper solid and long-dashed black curves show the parameters $p_{c\parallel}$ and $p_{h\parallel}$, which specify

the temperatures $T_{\text{eff}c\parallel}$ and $T_{\text{eff}h\parallel}$, respectively. The lower solid and long-dashed black curves show the relative surface areas $s_{c\parallel}$ and $s_{h\parallel}$ of the colder and hotter surface regions. For the equator observations, $p_{c\perp}$ and $p_{h\perp}$ are plotted by the short-dashed and dotted upper grey lines, while $s_{c\perp}$ and $s_{h\perp}$ by similar lower grey lines.

For both panels in Fig. 5 we have $T_{\text{eff}h\parallel} \approx T_{\text{eff}h\perp}$ and $T_{\text{eff}c\parallel} \approx T_{\text{eff}c\perp}$. This is because the spectral fluxes are generally close to isotropic 1BB with given T_{eff} (Page 1995; also see Fig. 2). However, $T_{\text{eff}h}$ is noticeably higher than $T_{\text{eff}c}$, indicating that hotter and colder surface regions are distinctly pronounced in the spectra. Also, we have $s_{c\parallel} \approx s_{c\perp}$ and $s_{h\parallel} \approx s_{h\perp}$.

The dependence of fit parameters on T_{eff} is seen to be smooth and not too sensitive to B_{pole} . Systematically, $T_{\text{eff}h}$ is from 10 to

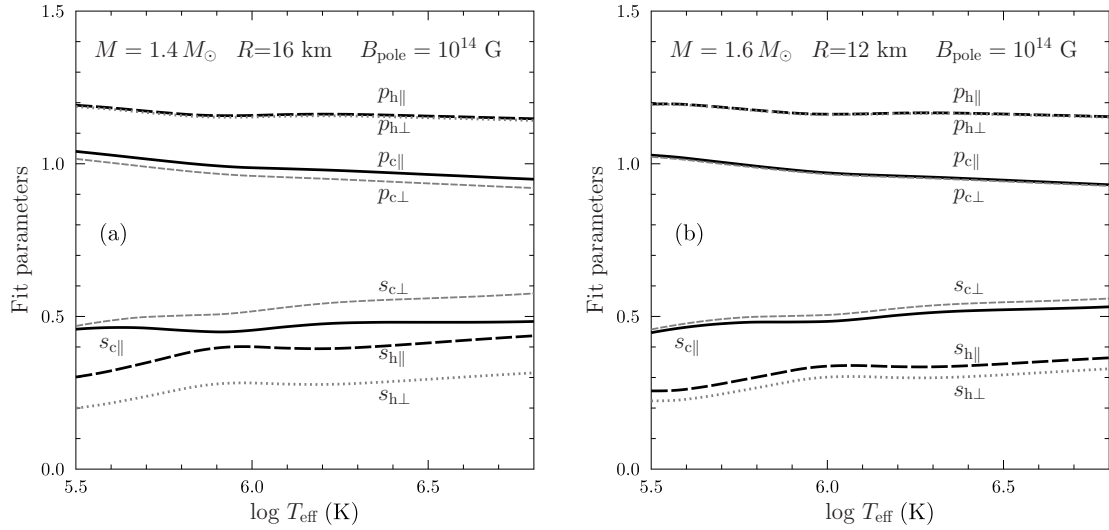


Figure 7. 2BB fit parameters versus $\log T_{\text{eff}}$ for a neutron star with $B_{\text{pole}} = 10^{14}$ G (as in Fig. 5b at $M = 1.4 M_{\odot}$ and $R = 12$ km) but for different M and R . Panel (a) refers to a less compact star with $M = 1.4 M_{\odot}$ and $R = 16$ km. Panel (b) is for a more compact star with $M = 1.6 M_{\odot}$ and $R = 12$ km.

20 per cent higher than T_{effc} . In a colder star ($\log T_{\text{eff}} \sim 5.5$) one has $T_{\text{eff}} \approx T_{\text{effc}}$, but for a hotter star ($\log T_{\text{eff}} \gtrsim 6.5$) $T_{\text{eff}} \approx T_{\text{effh}}$. The dependence of the fractional areas s_c and s_h on the observation angle is stronger than for p_c and p_h .

Fig. 6 shows the behavior of the same 2BB fit parameters, as in Figs. 5 ($M = 1.4 M_{\odot}$, $R = 12$ km), but versus B_{pole} at $\log T_{\text{eff}}[\text{K}] = 6.4$ [panel (a)] and 5.8 [panel (b)]. The dependence of fit parameters on B_{pole} is weak. For instance, B_{pole} varies over 3.5 orders of magnitude in Fig. 6 but the fit parameters vary much less.

Fig. 7 shows the same 2BB fit parameters versus T_{eff} at $B_{\text{pole}} = 10^{14}$ G, as in Fig. 5b, but for other values of M and R . Fig. 7a refers to a less compact star ($M = 1.4 M_{\odot}$, $R = 16$ km, smaller M/R), while Fig. 7b is for a more compact star, with $M = 1.6 M_{\odot}$ and $R = 12$ km. The overall behavior of the curves in panel (b) is similar to that in panel (a). Generally, the parameters p on panel (b) are less affected by the stellar compactness than the parameters s . The stronger the compactness, the smaller the difference between the fit parameters for the pole and equator observations, making the thermal radiation more uniform due to stronger general relativistic (GR) effects. This was shown by Page (1995) by direct calculations of some spectral fluxes.

Let us stress that we have fitted *unabsorbed* computed spectral fluxes by *unabsorbed* 2BB models. In this way we have established one-to-one theoretical correspondence between the two models. On the other hand, observational data allow observers (in principle) to infer 2BB emission parameters, which are corrected for interstellar absorption, for a possible existence of non-thermal radiation component and similar effects. If so, we can compare these observational data with the parameters given by our unabsorbed 2BB models considered here.

So far we have studied 2BB maps for neutron stars with heat blankets of iron (e.g. Potekhin et al. 2003; Beznogov et al. 2021). As a test, we have constructed a 2BB map for the star with $M = 1.4 M_{\odot}$, $R = 12$ km and $B_{\text{pole}} = 10^{14}$ G versus $\log T_{\text{eff}}$ using the blanket composed of accreted matter. We do not present the plot; it looks similar to that in Fig. 5b.

3.5 Phase-resolved spectroscopy

Phase-resolved spectroscopy from magnetized spherical neutron stars with dipole magnetic fields in the surface layers was extensively studied by Page (1995) by calculating a number of phase-resolved spectra.

We could do the same using our 2BB fits to the spectral fluxes for the pole and equator observations and composing the fluxes for any observation direction (Sect. 3.3). The results would be similar. Some differences would stem from using somewhat more refined surface temperature distribution (Potekhin et al. 2007) than in Page (1995). We do not describe the details but refer to Page (1995) for an analysis of pulse fractions. For a star with $M = 1.4 M_{\odot}$, $R = 12$ km, $B_{\text{pole}} \sim 10^{12}$ G and $\log T_{\text{eff}}[\text{K}] \sim 5.6$ at $E \sim 3$ keV the maximum pulse fraction is about 10 per cent. It increases with the growth of B_{pole} , E , and R/M but decreases with the growth of T_{eff} . It could be significantly higher if one neglected the effects of light bending above the neutron star surface. Other models of emission from magnetized neutron stars including pulse resolved spectroscopy, more complicated field geometry and a possible presence of condensed surface, have been considered in many publications (e.g. Page & Sarmiento 1996; Pérez-Azorín et al. 2005; Geppert et al. 2006; Zane & Turolla 2006; Hambaryan et al. 2011; Popov et al. 2017; De Grandis et al. 2021).

3.6 Testing cold equatorial belt

So far we have studied spectral fluxes and their 2BB maps for one particular model (Sect. 2.2) of the surface temperature distribution $T_s(\vartheta)$, corresponding to a pure dipole magnetic field in the surface layer of the star. Obviously, realistic $T_s(\mathbf{n})$ distributions can be more complicated. For simplicity, we restrict ourselves to sufficiently weak axially symmetric variations of $T_s(\vartheta)$, which are symmetric also with respect to the magnetic equator.

The most doubtful place in our $T_s(\vartheta)$ distribution is a thin cold equatorial surface belt (Sect. 2.2, Fig. 1). The temperature is much lower there, than in other places of the surface. Because this temperature distribution was calculated (e.g. Beznogov et al. 2021)

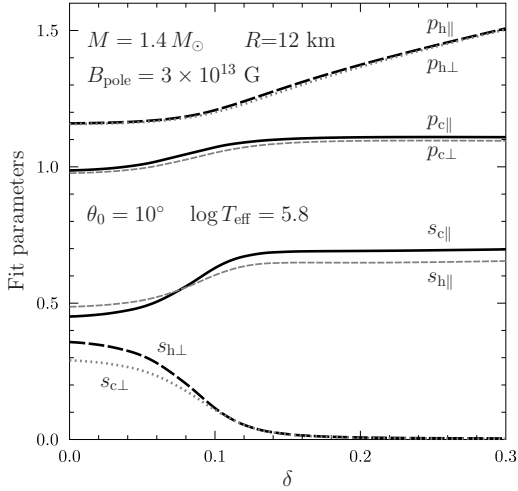


Figure 8. 2BB fit parameters for a neutron star with $M = 1.4 M_{\odot}$, $R = 12$ km, $\log T_{\text{eff}}[\text{K}] = 5.8$ and $B_{\text{pole}} = 3 \times 10^{13}$ G with extra hotspots of angular size $\vartheta_0 = 10^\circ$ on magnetic poles [described by equation (12)] versus extra relative surface temperature increase δ at the pole. See the text for details.

taking into account only the radial heat transport, the equatorial belt is the first place, where this $T_s(\vartheta)$ can be questioned. The heat can spread along the surface of the cold belt to the equator, reducing surface temperature variations there.

We have checked this effect on phenomenological level. We have taken a narrow equatorial surface strip of angular half-size $\delta\vartheta_{\text{belt}}$ and left the $T_s(\vartheta)$ dependence untouched outside this strip ($|\vartheta - \vartheta_{\text{eq}}| \geq \delta\vartheta_{\text{belt}}$, with $\vartheta_{\text{eq}} = 90^\circ$). Inside the strip, we have artificially assumed that $T_s(\vartheta) = (A - C \sin^2 \vartheta)^{1/4}$, where constants A and C have been chosen to ensure continuity of $T_s(\vartheta)$ and $\partial T_s / \partial \vartheta$ at $\vartheta = \vartheta_{\text{belt}} = \delta_{\text{eq}} - \delta_{\text{belt}}$. For $\delta\vartheta_{\text{belt}} = 30^\circ$, these profiles are shown by dotted lines in Fig. 1 (for the same values of T_{eff} as the standard solid lines, but using modified calculation of T_{eff} for the new profiles).

We have calculated modified spectral fluxes and 2BB maps for the same conditions, as in Fig. 5b, with two values $\delta\vartheta_{\text{belt}} = 10^\circ$ and 30° . In the first case the maps exactly coincided with the initial ones but the surface temperature still varied strongly over the belt. In the second case the T_s variations are greatly smoothed out (Fig. 1) but the maps appeared almost the same as the initial ones.

Therefore, variations of T_s in the cold equatorial belt seem to have almost no effect on the thermal surface emission (as has been anticipated earlier, e.g. [Beznogov et al. 2021](#)).

3.7 Warmer polar spots

Here we introduce two symmetric slightly warmer phenomenological spots on magnetic poles. Let $T_{s0}(\vartheta)$ be the local effective surface temperature given by our basic model (Sect. 2.2) and ϑ_0 be a small angle that determines the size of hotspots. We assume that

$$T_s(\vartheta) = T_{s0}(\vartheta) \left[1 + \delta \cos^2 \left(\frac{\pi \vartheta}{2\vartheta_0} \right) \right] \quad \text{at } \vartheta \leq \vartheta_0, \quad (12)$$

and that $T_s(\vartheta) = T_s(\vartheta_0)$ is not disturbed outside hotspots. The parameter δ determines a small extra temperature enhancement in the spot's center. This enhancement smoothly disappears as $\vartheta \rightarrow \vartheta_0$. The presence of spots renormalizes (slightly increases) the total effective temperature T_{eff} , equation (5).

Otherwise computations of spectral fluxes are the same as in Sect. 2.2. These fluxes can also be approximated by 2BB fits as in Sect. 3.1, and can be analyzed via phase-space maps. For the examples presented below the relative the fit accuracy becomes worse (reaching sometimes 10 per cent) but the fit is still sufficiently good and robust.

Fig. 8 plots the illustrative 2BB fit parameters versus δ for a star with $1.4 M_{\odot}$, $R = 12$ km, $B_{\text{pole}} = 3 \times 10^{13}$ G, $\log T_{\text{eff}}[\text{K}] = 5.8$ and hotspot angular size $\vartheta_0 = 10^\circ$. In the absence of hotspots ($\delta = 0$), the results are very close to those in Fig. 5b calculated at the same $\log T_{\text{eff}}[\text{K}] = 5.8$ (but for slightly higher $B_{\text{pole}} = 10^{14}$ G). However, when δ grows up, the fit parameters become different. The temperature T_{effh} of the hotter BB component and the effective emission surface area s_c of the colder BB component noticeably increase, whereas the emission surface area of the hotter component dramatically falls down. Even with really small hotspot temperature enhancement $\delta \gtrsim 0.15$ (equivalent to 0.6 per cent luminosity enhancement), we obtain qualitatively new phase-space portrait with $s_h \ll s_c$. Such 2BB fits have been often obtained from observations of cooling isolated neutron stars (see Sect. 4); these sources are usually interpreted as neutron stars with small hotspots.

Therefore, the theory predicts two types of neutron stars whose spectra are described by the 2BB models. The first ones are those with smooth surface temperature distributions, created by nonuniform surface magnetic fields and considered mainly throughout this paper. We will call these spectral models as 2BB *with smooth magnetic atmospheres*. The sources of the second type are those with distinct hotspot BB component. We will call them as 2BB *with hotspots*. Obviously, the sources of the two types are different but there is a smooth transition between them (for instance, by increasing δ in Fig. 8) meaning possible existence of the sources of intermediate type. Such a transition would require some extra heating in the hotter place of the magnetic atmosphere. According to Sect. 3.6, an extra heating of the colder equatorial belt would be less efficient.

4 DISCUSSION AND CONCLUSIONS

4.1 Candidates

Let us mention several candidates, among cooling isolated middle-aged neutron stars (not magnetars), which may demonstrate their multi-BB spectra as 2BB ones. We do not pretend to be complete, but give some examples. We base on the recent catalog ([Potekhin et al. 2020](#)) available also on the Web: [//www.ioffe.ru/astro/NSG/thermal/cooldat.html](http://www.ioffe.ru/astro/NSG/thermal/cooldat.html).

1. XMMU J172054.5–372652 is a neutron star that is probably associated with the SNR G350.1–0.3 (as suggested by [Gaensler et al. 2008](#)). There is no direct evidence of pulsations. [Lovchinsky et al. \(2011\)](#) presented arguments that the SNR G350.1–0.3 is freely expanding and estimated its age as ~ 1000 years. [Potekhin et al. \(2020\)](#) used archival *Chandra* data and fitted the X-ray spectrum with a neutron star (NSX) atmosphere model assuming $M = 1.4 M_{\odot}$ and $R = 13$ km. They obtained $T_{\text{eff}} \approx 2$ MK, but did not perform two-component fits which would be interesting.

2. PSR B1055–52 (J1057–5226) is a well known moderately magnetized middle-aged pulsar. Its effective magnetic field, as determined from the standard model of magnetic dipole braking and reported in the ATNF pulsar catalog ([Manchester et al. 2005](#)), is $B_{\text{eff}} = 1.1 \times 10^{12}$ G (at the equator of an imaginary star with $M = 1.4 M_{\odot}$ and $R = 10$ km). This value does not allow one to accurately determine B_{pole} but indicates that B_{pole} is roughly equals

a few times of 10^{12} G. Potekhin et al. (2020) presented the value $k_B T_{\text{eff}}^{\infty} \approx 70$ eV ($T_{\text{eff}}^{\infty} \approx 0.8$ MK). It is based on the 2BB spectral fit by De Luca et al. (2005) which included also a power-law (PL) non-thermal radiation component. Potekhin et al. (2020) have corrected the results by De Luca et al. (2005) for more plausible distance estimate to the source obtained by Mignani et al. (2010). The fit gives $T_{\text{effh}}/T_{\text{effc}} \sim 2.3$ and $s_h \ll s_c$. It agrees with a 2BB model containing hotspots.

3. PSR J1740+1000 has $B_{\text{eff}} = 1.8 \times 10^{12}$ G. The 2BB spectral fit was done by Kargaltsev et al. (2012). Taking the same version of the fit as selected by Potekhin et al. (2020), we again have $k_B T_{\text{eff}}^{\infty} \approx 70$ eV ($T_{\text{eff}}^{\infty} \approx 0.8$ MK), $T_{\text{effh}}/T_{\text{effc}} \sim 2.8$ and $s_h \ll s_c$, with the same conclusion as for the PSR B1055–52.

4. PSR B1823–13 (J1826–1334) is located in the SNR G18.0–00.7 and has $B_{\text{eff}} = 2.8 \times 10^{12}$ G. Its X-ray emission is mostly non-thermal (Pavlov et al. 2008; Zhu et al. 2011) but the PL fits suggest the presence of some thermal component. The 1BB+PL fit gives the radius of thermally emitting region $R_{\text{eff}}^{\infty} \approx 5$ km, that is smaller than a realistic radius of a neutron star. Adding the second BB component does not seem statistically sound with the present data but might be possible in the future.

5. RX J1605.3+3249 (RBS 1556) is a neutron star studied by many authors (e.g. Motch et al. 2005; Posselt et al. 2007; Tetzlaff et al. 2012; Pires et al. 2019; Malacaria et al. 2019) with contradictory conclusions on its distance and other properties (see Potekhin et al. 2020, for details). Its spin period has been found but later disproved by Pires et al. (2019). The timing and spectral analysis of X-ray emission have been performed under different assumptions using BB and neutron star atmosphere models. Recently Pires et al. (2019) have analysed the *XMM-Newton* observations. Also, Malacaria et al. (2019) performed a joint analysis of the *NICER* and *XMM-Newton* data. Both teams report improving of 2BB fits if one adds a broad Gaussian absorption line. In this case, they obtain $k_B T_{\text{effc}}^{\infty} \sim 60$ eV ($T_{\text{effc}}^{\infty} \sim 0.7$ MK), and $T_{\text{effh}}/T_{\text{effc}} \sim 2$. This can be the 2BB case with not very warm spots, where the effects of smooth magnetic atmosphere are not negligible.

6. RX J1856.5–3754 is a neutron star with nearly thermal spectrum. It was discovered by Walter, Wolk & Neuhäuser (1996). It is slowly rotating, with the spin period of about 7 s; its effective magnetic field is $B_{\text{eff}} \sim 1.5 \times 10^{13}$ G (although magnetic field properties are still highly debated; e.g. Popov et al. 2017; De Grandis et al. 2021 and references therein). Its spectrum has been measured in a wide range of wavelengths, including X-rays, optical and radio. It has been interpreted with a number of spectral models, particularly, with the model of thin partially ionized magnetized hydrogen atmosphere on top of solidified iron surface (e.g., Ho et al. 2007; Potekhin 2014). Note alternative 2BB, 2BB+PL, and 3BB fits constructed by Sartore et al. (2012) and Yoneyama et al. (2017). In particular, the 2BB fits give $k_B T_{\text{effc}}^{\infty} \sim 40$ eV ($T_{\text{effc}}^{\infty} \approx 0.46$ MK), $T_{\text{effh}}/T_{\text{effc}} \sim 1.6$, $R_{\text{effh}} \sim 0.5R$ and $R_{\text{effc}} \sim R$. These 2BB fits look closer to the 2BB spectral models with smooth magnetic atmosphere, than other 2BB fits described above. Introducing warmer spots simplifies this interpretation.

In summary, if 2BB spectral fits are done, they can give a hint on a possible importance of localized hotspots or smooth variations of the surface temperature. For refining this interpretation, it would be better to use more advanced models of neutron star atmospheres (e.g. Ho et al. 2008; Zyuzin et al. 2021).

4.2 Conclusions

We have studied simple models (Sect. 2) of thermal spectra emitted from surfaces of spherical isolated neutron stars with dipole surface magnetic fields $10^{11} \lesssim B_{\text{pole}} \lesssim 10^{14}$ G. Such fields make the surface temperature distribution noticeably non-uniform. The model assumes BB radiation with a local temperature from any surface element, meaning multi-BB emission as a whole. The model properly treats the GR effects as well as variations of temperature and magnetic fields over the surface (such as colder equatorial belts and hotter magnetic poles).

We have shown that these multi-BB radiation spectra are accurately fitted by 2BB models for all observation directions by specifying eight fit parameters (temperatures and effective emitting areas of colder and hotter BB components for pole and equator observations) at any given set of values of B_{pole} , T_{eff} , M and R . For example, Table 1 presents fit parameters for a star with $M = 1.4 M_{\odot}$ and $R = 12$ km on a grid of B_{pole} and T_{eff} values. We can easily generate such tables for any values of input parameters. We have studied the so called 2BB portraits of neutron star emission, which give the dependence of fit parameters on input phase-space ones (B_{pole} , T_{eff} , etc.). Comparing these theoretical 2BB maps with 2BB fits, inferred from the observed spectra, gives a method of estimating the magnetic field properties on neutron star surface.

Next we show (Sect. 3.6) that a possible extra heating of cold equatorial surface belt by heat flows from neighboring warmer surface regions does not have strong impact on theoretical 2BB maps. In contrast, even slight extra heating of magnetic poles can strongly affect the radiation spectra but does not violate the 2BB approximation (Sect. 3.7). It increases the effective temperature T_{effh} of the hotter BB component, strongly reduces the fractional emission area s_h of this component, drastically changes 2BB maps and realizes a transition to 2BB emission with hotspots. The latter regime is quite known from observations. We have mentioned some cooling neutron stars which emit as 2BB with hotspots or as 2BB transiting between hot spots and smooth magnetic atmospheres (Sect. 4.1.)

Our consideration is restricted by studying dipole-like surface magnetic fields. Actual fields can be more complicated and the assumption that any surface element radiates as a BB can be violated, but such effects go beyond the scope of this paper. However, the present consideration can be extended to more sophisticated field geometries and the 2BB approximation can be a proper tool for theoretical interpretations of these observations as well.

ACKNOWLEDGMENTS

I am grateful to the anonymous referee for constructive critical remarks. This research was partly supported by the grant 14.W03.31.0021 of the Ministry of Science and Higher Education of the Russian Federation and by the travel grants 316932 and 332666 of the Academy of Finland.

DATA AVAILABILITY

The data underlying this article will be shared on reasonable request to the corresponding author.

References

Beloborodov A. M., 2002, *ApJ*, 566, L85

- Beznogov M. V., Potekhin A. Y., G. Y. D., 2021, *Physics Reports*, 919, 1
- De Grandis D., Taverna R., Turolla R., Gnarini A., Popov S. B., Zane S., Wood T. S., 2021, arXiv e-prints, p. arXiv:2105.00684
- De Luca A., Caraveo P. A., Mereghetti S., Negroni M., Bignami G. F., 2005, *ApJ*, **623**, 1051
- Gaensler B. M., et al., 2008, *ApJ*, **680**, L37
- Geppert U., Küker M., Page D., 2006, *A&A*, 457, 937
- González Caniulef D., Zane S., Taverna R., Turolla R., Wu K., 2016, *MNRAS*, 459, 3585
- Greenstein G., Hartke G. J., 1983, *ApJ*, **271**, 283
- Hambaryan V., Suleimanov V., Schwöpe A. D., Neuhäuser R., Werner K., Potekhin A. Y., 2011, *A&A*, **534**, A74
- Ho W. C. G., Kaplan D. L., Chang P., van Adelsberg M., Potekhin A. Y., 2007, *MNRAS*, **375**, 821
- Ho W. C. G., Potekhin A. Y., Chabrier G., 2008, *ApJS*, **178**, 102
- Kargaltsev O., Durant M., Misanovic Z., Pavlov G. G., 2012, *Science*, **337**, 946
- Lovchinsky I., Slane P., Gaensler B. M., Hughes J. P., Ng C. Y., Lazendic J. S., Gelfand J. D., Brogan C. L., 2011, *ApJ*, **731**, 70
- Malacaria C., et al., 2019, *ApJ*, **880**, 74
- Manchester R. N., Hobbs G. B., Teoh A., Hobbs M., 2005, *AJ*, **129**, 1993
- Mignani R. P., Pavlov G. G., Kargaltsev O., 2010, *ApJ*, **720**, 1635
- Motch C., Sekiguchi K., Haberl F., Zavlin V. E., Schwöpe A., Pakull M. W., 2005, *A&A*, **429**, 257
- Page D., 1995, *ApJ*, **442**, 273
- Page D., Sarmiento A., 1996, *ApJ*, 473, 1067
- Pavlov G. G., Kargaltsev O., Briskin W. F., 2008, *ApJ*, **675**, 683
- Pérez-Azorín J. F., Miralles J. A., Pons J. A., 2005, *A&A*, 433, 275
- Pires A. M., Schwöpe A. D., Haberl F., Zavlin V. E., Motch C., Zane S., 2019, *A&A*, **623**, A73
- Popov S. B., Taverna R., Turolla R., 2017, *MNRAS*, 464, 4390
- Posselt B., Popov S. B., Haberl F., Trümper J., Turolla R., Neuhäuser R., 2007, *Ap&SS*, **308**, 171
- Potekhin A. Y., 2014, *Phys. Usp.*, 57, 735
- Potekhin A. Y., Chabrier G., 2018, *A&A*, 609, A74
- Potekhin A. Y., Yakovlev D. G., 2001, *A&A*, **374**, 213
- Potekhin A. Y., Yakovlev D. G., Chabrier G., Gnedin O. Y., 2003, *ApJ*, 594, 404
- Potekhin A. Y., Chabrier G., Yakovlev D. G., 2007, *Astrophys. Space Sci.*, **308**, 353
- Potekhin A. Y., De Luca A., Pons J. A., 2015a, *Space Sci. Rev.*, 191, 171
- Potekhin A. Y., Pons J. A., Page D., 2015b, *Space Sci. Rev.*, 191, 239
- Potekhin A. Y., Zyuzin D. A., Yakovlev D. G., Beznogov M. V., Shibbanov Y. A., 2020, *MNRAS*, 496, 5052
- Poutanen J., 2020, *A&A*, 640, A24
- Poutanen J., Gierliński M., 2003, *MNRAS*, 343, 1301
- Sartore N., Tiengo A., Mereghetti S., De Luca A., Turolla R., Haberl F., 2012, *A&A*, **541**, A66
- Tetzlaff N., Schmidt J. G., Hohle M. M., Neuhäuser R., 2012, *Publ. Astron. Soc. Australia*, **29**, 98
- Walter F. M., Wolk S. J., Neuhäuser R., 1996, *Nature*, **379**, 233
- Yoneyama T., Hayashida K., Nakajima H., Inoue S., Tsunemi H., 2017, *PASJ*, **69**, 50
- Zane S., Turolla R., 2006, *MNRAS*, 366, 727
- Zavlin V. E., Pavlov G. G., 2002, in Becker W., Lesch H., Trümper J., eds, *Neutron Stars, Pulsars, and Supernova Remnants*. p. 263 ([arXiv:astro-ph/0206025](https://arxiv.org/abs/astro-ph/0206025))
- Zhu W. W., Kaspi V. M., McLaughlin M. A., Pavlov G. G., Ng C. Y., Manchester R. N., Gaensler B. M., Woods P. M., 2011, *ApJ*, **734**, 44
- Zyuzin D. A., Karpova A. V., Shibbanov Y. A., Potekhin A. Y., Suleimanov V. F., 2021, *MNRAS*, 501, 4998